Ocean Dynamics (2013) 63:881–900
DOI 10.1007/s10236-013-0631-3

An integrated East China Sea–Changjiang Estuary model system with aim at resolving multi-scale regional–shelf–estuarine dynamics

Jianzhong Ge · Pingxing Ding · Changsheng Chen · Song Hu · Gui Fu · Lunyu Wu

Received: 5 August 2012 / Accepted: 3 June 2013 / Published online: 28 June 2013

Abstract A high-resolution numerical model system is essential to resolve multi-scale coastal ocean dynamics. So a multi-scale unstructured grid-based finite-volume coastal ocean model (FVCOM) system has been established for the East China Sea and Changjiang Estuary (ECS–CE) with the aim at resolving coastal ocean dynamics and understanding different physical processes. The modeling system consists of a three-domain-nested weather research and forecasting model, FVCOM model with the inclusion of FVCOM surface wave model in order to understand the wave–current interactions. The ECS–CE system contains three different scale models: a shelf-scale model for the East China Sea, an estuarine-scale model for the Changjiang Estuary and adjacent region, and a fine-scale model for the deep waterway regions. These three FVCOM-based models guarantee the conservation of mass and momentum transferring from outer domain to inner domain using the one-way common-grid nesting procedure. The model system has been validated using data from various observation data, including surface wind, tides, currents, salinity, and wave to accurately reveal the multi-scale dynamics of the East China Sea and Changjiang Estuary. This modeling system has been demonstrated via application to the seasonal variations of Changjiang diluted water and the bottom saltwater intrusion in the North Passage, and it shows strong potential for estuarine and coastal ocean dynamics and operational forecasting.

Keywords Multi-scale dynamics · FVCOM · Changjiang Estuary · East China Sea

Responsible Editor: Emil Vassilev Stanev

J. Ge (✉) · P. Ding · C. Chen
The State Key Laboratory of Estuarine and Coastal Research, East China Normal University, 3663 North Zhongshan Road, Shanghai 200062, China
e-mail: jzge@sklec.ecnu.edu.cn

P. Ding
e-mail: pxding@sklec.ecnu.edu.cn

C. Chen
e-mail: c1chen@umassd.edu

C. Chen
School for Marine Science and Technology, University of Massachusetts—Dartmouth, New Bedford, MA 02744, USA

S. Hu
College of Marine Sciences, Shanghai Ocean University, Shanghai 201306, People's Republic of China
e-mail: shu@shou.edu.cn

G. Fu
Yangtze Estuary Waterway Administration Bureau, Ministry of Communication, Shanghai 200003, People's Republic of China
e-mail: glss456@qq.com

L. Wu
The First Institute of Oceanography, State Ocean Administration, Qingdao 266061, People's Republic of China
e-mail: wuly@fio.org.cn

1 Introduction

Changjiang Estuary is located in the west boundary of the East China Sea (ECS) shelf, characterized by abundant supplies of freshwater discharges and sediment from the Changjiang River (CR), which is the largest river discharging into the ECS (Fig. 1), with an annual average freshwater discharge of 28,527 m^3/s and peak value above 50,000 m^3/s during flooding season (Chen et al. 1999; Ge et al. 2012). The strong freshwater discharge from the Changjiang River during summer also

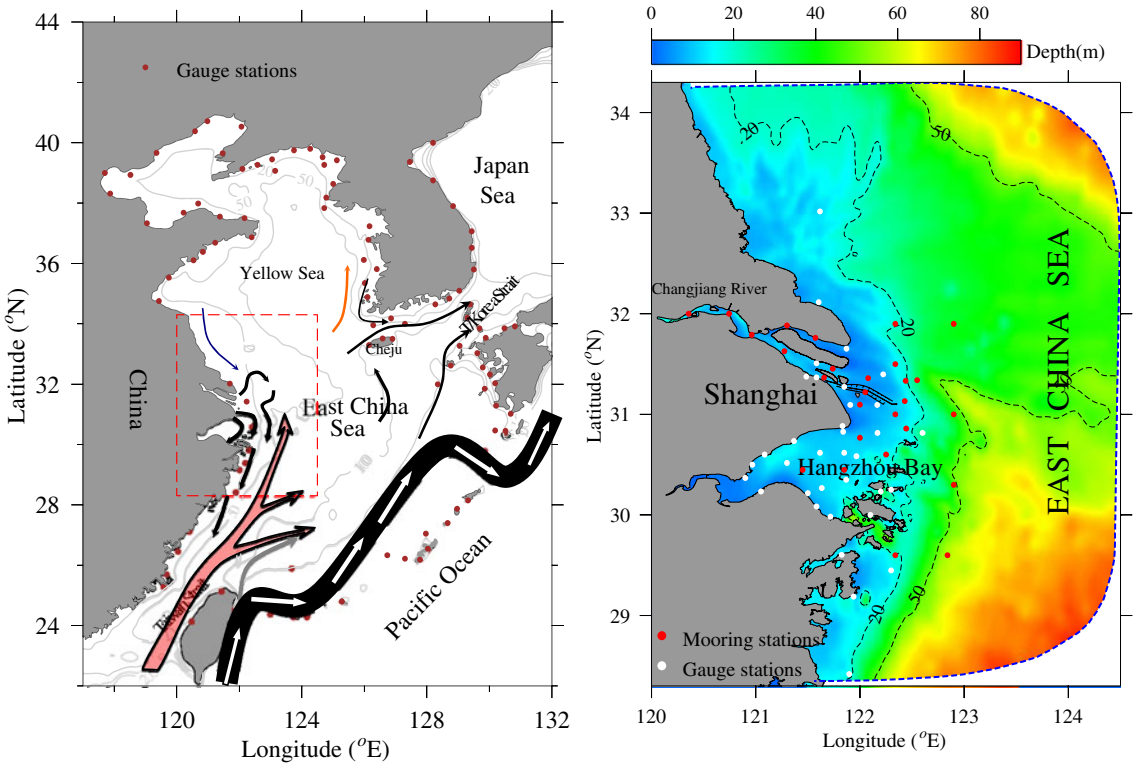

Fig. 1 Bathymetry distributions of the East China Sea shelf (*left*) and the Changjiang Estuary (*right*). The *thick-black*, *yellow*, and *blue arrows* indicate the Kuroshio Current, Taiwan Warm Current, and Jiangsu alongshore current, respectively. The *thin black arrows in the dashed box* indicate the Changjiang Diluted Water Current. The *magenta points in the left panel* indicate the gauge stations along the coasts of the East China Sea, Yellow Sea, Bohai Sea, and Japan Sea. The *red points* show the mooring stations used for model validation, and the *white points* (geographic coordinates listed in the text) indicate the gauge stations around Changjiang Estuary

creates a low-salinity plume around the estuary and the inner shelf of the ECS. During the flooding summertime, the Changjiang dilute water mainly has three branches, one merged into the adjacent Hangzhou Bay, one turned clockwise and produced significant along-shelf current with southward direction, and last one flows northeastern under the combined effect of vortex stretching, monsoon-driven offshore advection, and internal baroclinic instability (Beardsley et al. 1985; Chang and Isobe 2003; Lie et al. 2003; Chen et al. 2008; Wu et al. 2011a).

The Shelf of East China Sea is a typical buffer zone: It is not only under the direct impact of Taiwan Warm Current and remote control of the Kuroshio water intrusion into the shelf but also significantly controlled by seasonal variation Changjiang dilute water (Beardsley et al. 1985; Isobe and Matsuno 2008; Li et al. 2006; Chen et al. 2008). The Kuroshio mainly flows along the shelf break with continuous intrusion into the shelf slope. The Taiwan Warm Current enters into the East China Sea shelf along the shelf boundary, with several sub-branches into the inner shelf and outer region (Chen et al. 2003b; Zhu et al. 2004; Sasaki et al. 2008).

In additional, Changjiang Estuary and adjacent shelf region is the main region of significant interaction of multi-scale dynamics. The distribution, propagation, and breakdown of the plume water are significantly influenced by the shelf circulation, especially related to the Taiwan Warm Current (TWC) (Beardsley et al. 1985; Hu et al. 2002; Chen et al. 2008; Wu et al. 2011a). The shelf-scale TWC reaches the 30–40-m isobath regions and produces high-salinity intrusion into the Changjiang Estuary. And the freshwater discharge into the East China Sea shelf plays a critical role on the shelf-scale mass transport. The numerical and drifter experiment indicates that the plume water could be advected to the Cheju region, then float into the Japan/East Sea through Tsushima/Korea Strait (Beardsley et al. 1992).

Therefore, the multi-scale dynamics needs to be correctly resolved by a numerical estuarine and coastal model through reproducing regional–shelf–estuarine circulation. This potentially requires a model system with the capability of wide geographic coverage from regional oceanic influences into local estuarine dynamics and of high spatial resolution around local region.

In the previous researches, multi-scale dynamics around the Changjiang Estuary have been conducted: With the help of one-way nesting method, Hu et al. (2004) included the typhoon-induced surface elevation propagation from East China Sea shelf to Changjiang Estuary and Hangzhou Bay to consider the effect

of the coastal ocean to the nearshore storm surge. The dynamic variations of coastal and nearshore around the Changjiang Estuary were also studied by Delcroix and Murtugudde (2002), Chang and Isobe (2003), Guo et al. (2006), Qiao et al. (2006), Watanabe (2007), Moon et al. (2010), Wu et al. (2011a), etc. These works were mainly conducted using coastal ocean model such as Princeton ocean model (POM), estuarine and coastal ocean model, and regional ocean model system (ROMS) with curvilinear orthogonal grids. Moreover, previous researches were mainly process-oriented studies, and did not include the interaction of local and regional dynamics (Chen et al. 2008). Thus, a forecast model system is potentially required with a focus on the Changjiang Estuary and the consideration of the outer East China Sea shelf, which has not been done in previous work.

The integrated model system has been increasingly developed and applied to the coastal ocean research and forecast, such as POM-based ones (Moon 2005; Onken et al. 2005), hybrid coordinate ocean model (HYCOM)-based (Chassignet et al. 2007; Barth et al. 2008), ROMS-based (Haidvogel et al. 2008; Chao et al. 2009; Weisberg et al. 2009; Powell et al. 2009; Warner et al. 2010; Olabarrieta et al. 2012), and other model-based system (Lane et al. 2009; Schmidt and Gangopadhyay 2012). These orthogonal grid model included multiple dynamics such circulation, tide, wave, and sediment with high efficiency of computation. However, orthogonal-grid-nesting interpolation has difficulty in resolving multi-scale dynamics with non-conservation issue of mass and momentum. So model systems based on unstructured-grid finite-volume coastal ocean model (FVCOM) with excellent downscaling capability have been gradually applied and developed, such as west Florida modeling system (Zheng and Weisberg 2012) and atmosphere–ocean–wave Northeast Coastal Ocean Forecast System (http://fvcom.smast.umassd.edu/research_projects/NECOFS).

In this paper, we developed a high-resolution unstructured-grid FVCOM model system addressing interactions of multi-scale dynamics: a shelf-scale East China Sea model, an estuarine-scale Changjiang model, and a fine-scale deep waterway model. The model system was well validated with the observation data of atmosphere, tide, current, wave, and salinity. Then it has been applied to simulate the seasonal spreading of the Changjiang plume waters and the bottom saltwater intrusion during summer within the North Passage.

This paper is organized as follows: The framework, numerical skills, and development of the high-resolution unstructured grid model system including three sub-domain models are described in Section 2; in Section 3, the model validations for tides, salinity, and currents around the Changjiang Estuary and adjacent regions are presented; Section 4 demonstrated the model system via two examples of applications. The discussion and conclusion are summarized in Section 5.

2 Development of the integrated model system

An integrated numerical model system has been developed with the aim at resolving multi-scale dynamics of the regional ECS shelf and local Changjiang Estuary and adjacent regions. It is based on FVCOM, which is a prognostic, unstructured-grid, finite-volume, free-surface, 3-D primitive equation coastal ocean circulation model, and it consists of momentum, continuity, temperature, salinity, and density equations and is closed physically and mathematically using turbulence closure submodels. The horizontal grid is comprised of unstructured triangular cells, and the irregular bottom is presented using generalized terrain-following coordinates. FVCOM is solved numerically by a second-order accurate discrete flux calculation in the integral form of the governing equations over an unstructured triangular grid (Chen et al. 2003a, 2006a, b, 2007).

This model system consists of four parts: (a) regional and local weather research and forecasting models (WRF); (b) a regional and local FVCOM, which is a three-dimensional unstructured grid primitive equation ocean model with hydrostatic and non-hydrostatic solvers; (c) an unstructured grid FVCOM surface wave (SWAVE) model modified from the orthogonal grid SWAN model. The circulation models contain three sub-domain models: a regional East China Sea FVCOM, a Changjiang Estuary FVCOM, and a deep waterway FVCOM (Fig. 2). The core modules and these multi-scale models are described below.

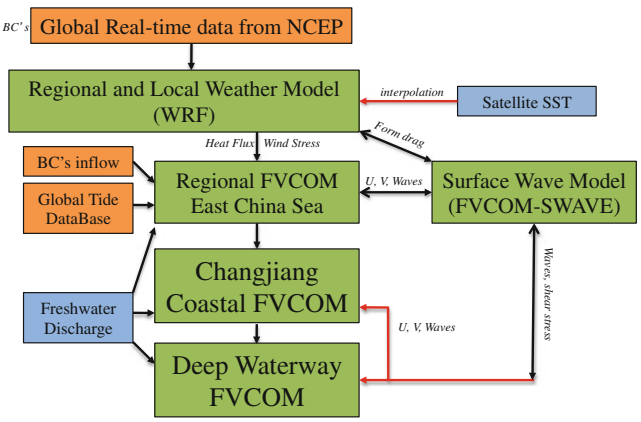

Fig. 2 Framework of the multi-scale FVCOM-based model system, including the regional East China Sea FVCOM, coastal Changjiang Estuary FVCOM, and local deep waterway FVCOM and their related internal and external models and modules

2.1 Wave–current coupled module

In a generalized terrain-following coordinate system, the governing equations of momentum, continuity, temperature, salinity, and density with the inclusion of three-dimensional radiation stress are given as follows:

$$\begin{aligned}&\frac{\partial uD}{\partial t}+\frac{\partial u^2D}{\partial x}+\frac{\partial uvD}{\partial y}+\frac{\partial u\omega}{\partial\widehat{\sigma}}-fvD\\&=-D\frac{\partial}{\partial x}(g\eta+p_{\mathrm{atm}})-D\int_{\widehat{\sigma}}^{0}\left(D\frac{\partial\rho}{\partial x}-\widehat{\sigma}\frac{\partial D}{\partial x}\frac{\partial\rho}{\partial\widehat{\sigma}}\right)d\widehat{\sigma}\\&-\left(\frac{\partial DS_{xx}}{\partial x}+\frac{\partial DS_{xy}}{\partial y}\right)+\widehat{\sigma}\left(\frac{\partial D}{\partial x}\frac{\partial S_{xx}}{\partial\widehat{\sigma}}+\frac{\partial D}{\partial y}\frac{\partial S_{xy}}{\partial\widehat{\sigma}}\right)+\frac{\partial\tau_x}{\partial\widehat{\sigma}}\end{aligned}\tag{1}$$

$$\begin{aligned}&\frac{\partial vD}{\partial t}+\frac{\partial uvD}{\partial x}+\frac{\partial v^2D}{\partial y}+\frac{\partial v\omega}{\partial\widehat{\sigma}}+fuD\\&=-D\frac{\partial}{\partial y}(g\eta+p_{\mathrm{atm}})-D\int_{\widehat{\sigma}}^{0}\left(D\frac{\partial\rho}{\partial y}-\widehat{\sigma}\frac{\partial D}{\partial y}\frac{\partial\rho}{\partial\widehat{\sigma}}\right)d\widehat{\sigma}\\&-\left(\frac{\partial DS_{xy}}{\partial x}+\frac{\partial DS_{yy}}{\partial y}\right)+\widehat{\sigma}\left(\frac{\partial D}{\partial x}\frac{\partial S_{xy}}{\partial\widehat{\sigma}}+\frac{\partial D}{\partial y}\frac{\partial S_{yy}}{\partial\widehat{\sigma}}\right)+\frac{\partial\tau_y}{\partial\widehat{\sigma}}\end{aligned}\tag{2}$$

$$\frac{\partial Du}{\partial x}+\frac{\partial Dv}{\partial y}+\frac{\partial\omega}{\partial\widehat{\sigma}}+\frac{\partial\eta}{\partial t}=0\tag{3}$$

$$\frac{\partial\theta D}{\partial t}+\frac{\partial\theta uD}{\partial x}+\frac{\partial\theta vD}{\partial y}+\frac{\partial\theta\omega}{\partial\widehat{\sigma}}=\frac{1}{D}\frac{\partial}{\partial\widehat{\sigma}}\left(K_{\mathrm{h}}\frac{\partial\theta}{\partial\widehat{\sigma}}\right)+D\widehat{H}+DF_\theta\tag{4}$$

$$\frac{\partial sD}{\partial t}+\frac{\partial suD}{\partial x}+\frac{\partial svD}{\partial y}+\frac{\partial s\omega}{\partial\widehat{\sigma}}=\frac{1}{D}\frac{\partial}{\partial\widehat{\sigma}}\left(K_{\mathrm{h}}\frac{\partial s}{\partial\widehat{\sigma}}\right)+DF_{\mathrm{s}}\tag{5}$$

$$\rho=\rho(\theta,s),\tag{6}$$

where x, y, and $\widehat{\sigma}$ are the east, north, and vertical axes of the generalized terrain-following coordinate; t the time; u, v, and ω the x, y, and $\widehat{\sigma}$ components of the velocity; τ_x and τ_y the x and y components of the stress; η the sea surface elevation; h the mean water depth; $D=h+\eta$ the total water depth; θ the potential temperature; s the salinity; ρ the density; p_{atm} the air pressure; f the Coriolis parameter; $\widehat{H}$ the solar irradiance; and K_{h} the thermal vertical eddy diffusion coefficient; F_θ and F_{s} represent the thermal and salt diffusion terms. S_{xx}, S_{xy}, S_{xy}, and S_{yy} are the x and y components of the wave-induced radiation stress given as

$$\begin{aligned}S_{xx}&=kE\left(\frac{k_xk_x}{k^2}F_{\mathrm{CS}}F_{\mathrm{CC}}+F_{\mathrm{CS}}F_{\mathrm{CC}}-F_{\mathrm{CS}}F_{\mathrm{SS}}\right)+\frac{k_xk_x}{k}\frac{c^2}{L}A_RR_z,\\S_{yy}&=kE\left(\frac{k_yk_y}{k^2}F_{\mathrm{CS}}F_{\mathrm{CC}}+F_{\mathrm{CS}}F_{\mathrm{CC}}-F_{\mathrm{SC}}F_{\mathrm{SS}}\right)+\frac{k_yk_y}{k}\frac{c^2}{L}A_RR_z,\\S_{xy}&=S_{yx}=kE\left(\frac{k_xk_y}{k^2}F_{\mathrm{CS}}F_{\mathrm{CC}}\right)+\frac{k_xk_y}{k}\frac{c^2}{L}A_R\ R_z\ ,\end{aligned}\tag{7}$$

where E is the wave energy computed by

$$E=\frac{1}{16}gH_s^2,\tag{8}$$

The terms in brackets are momentum flux terms induced by waves (Mellor 2005), and the last terms are induced by surface boundary-layer rollers (Svendsen 1984; Svendsen et al. 2002; Warner et al. 2008), with a vertical distribution expressed as

$$R_z=1-\tanh\left(\frac{2s}{\gamma}\right)^4\tag{9}$$

where R_z vertically distributes the additional stress term due to the roller as an exponentially function decaying with depth and γ is the ratio of wave height to water depth ($\gamma=H_s/D$). c is wave-propagation speed. The roller area is determined on a formulation from (Svendsen 1984):

$$A_R=\frac{\alpha}{\sqrt{2}}H_{\mathrm{s}}LQ_{\mathrm{b}}\tag{10}$$

where α is a parameter with value 0.06 and Q_{b} is the friction of breaking waves.and

$$F_{\mathrm{SC}}=\frac{\sinh k(z+h)}{\cosh kD},\ F_{\mathrm{CC}}=\frac{\cosh k(z+h)}{\cosh kD},\tag{11}$$

$$F_{\mathrm{SS}}=\frac{\sinh k(z+h)}{\sinh kD},\ F_{\mathrm{CS}}=\frac{\cosh k(z+h)}{\sinh kD},\tag{12}$$

H_s, k, k_x, and k_y are the significant wave height, wave number, wave number in x-direction, and wave number in y-direction, respectively. These variables are computed from FVCOM-SWAVE described in Qi et al. (2009) and Wu et al. (2011b). Equations (7) and (8) indicate that the vertical radiation stresses are calculated via wave energy, which is simplified from truncated surface wave model.

2.2 Common-grid nesting module

Downscaling simulation is a practical solution for oceanic circulation for resolving multi-scale dynamics (Cailleau et al. 2008). One-way offline nesting technique is widely used in this downscaling modeling (Penven et al. 2006) to transfer

the mass and momentum of outer domain to internal domain. Typical nesting procedure for curvilinear grid is shown in Fig. 3a. The big domain covers the boundary of small domain, and the hydrodynamic information, such as surface elevation, current, salinity, and temperature, are transferred from big domain with interpolation method. However, since the bathymetry and geographic coordinate could not be identical between small and big domains. The interpolation method would produce some numerical error and generate some fake noise along the nesting boundary. Although various methods are developed to reduce nesting errors (Cailleau et al. 2008; Mason et al. 2010), the conservation of mass and momentum along the nesting boundary is still difficult to be guaranteed.

For unstructured triangle grid, it is capable of arbitrary resolution and adequate geographic coverage. It could avoid the nesting problem between multiple domains of structured grids. However, the computation load will significantly increase since all triangle grid shares the same external and internal time steps. Therefore, coarse and find grids with different time steps will potentially improve the modeling efficiency.

The one-way common-grid nesting procedure is presented in this paper to improve overall efficiency and guarantee the mass and momentum between the big and small domains. The sketch of triangle grids for nesting domains is shown in Fig. 3b. The big domain of coarse grid and small domain of fine grid share a same layer of nodes and cells, which forms the common grids between the nesting domains. The common grids in big domain have the identical geographic coordinates and depth values as small domains.

For one-way offline nesting simulation, the big domain saves all hydrodynamic variables, such as surface elevation, horizontal and vertical velocities, salinity, and temperature. These variables will be used to drive the small domain. This is a one-way nesting approach from big domain to small ones. Since this common-grid nesting does not need additional interpolation or extrapolation procedure along the nesting boundary, the conservation of mass and momentum is guaranteed.

In the vertical direction, the identical distribution of vertical layers and levels is required to avoid interpolation or extrapolation calculation for mass and momentum conservation. Therefore, the numbers of vertical layers and their thickness should be the same between big and small domains. The parameters controlling the σ-coordinate or s-coordinate are also needed to be identical during the nested running.

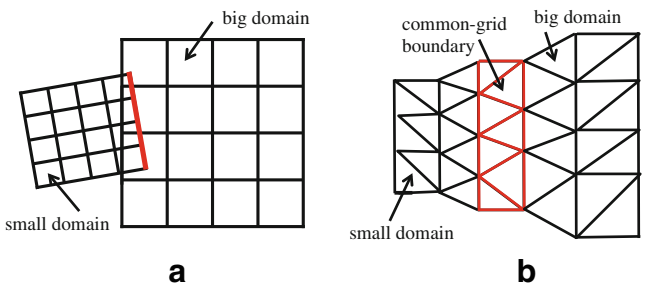

Fig. 3 Sketch of nesting methods for curvilinear orthogonal grid (**a**) and unstructured grid (**b**)

2.3 Regional and local weather model

A WRF model (Skamarock et al. 2008) is applied to set up a three-level regional model to cover basin, shelf, and regional geographic scales. Three WRF domains are shown in Fig. 4. The basin domain covers the entire East China Sea Shelf, Northwest Pacific Ocean, Japan Sea, and part of the South China Sea (Fig. 4a); the shelf domain has a geographic coverage including the Bohai Sea, Yellow Sea, East China Sea, Taiwan Strait, and Kuroshio region (Fig. 4b); and the regional domain covers the Changjiang Estuary, Hangzhou Bay, and adjacent landscape and oceanic regions (Fig. 4c). The domains have resolutions of 81, 27, and 9 km in the basin, shelf, and regional domains, respectively. This basin-shelf-scale WRF has the ability to provide the necessary surface forcing, such as 10-m-height wind, heat flux, and air pressure, for modeling of shelf, regional, and local circulation.

A two-way nesting method is employed during WRF computation (Michalakes et al. 2004). The model includes 31 vertical sigma levels from the earth surface, and the thicknesses of these sigma layers are dependent on the reference state pressure.

2.4 Regional East China Sea FVCOM

The regional East China Sea FVCOM (ECS-FVCOM) was originally designed by Chen et al. (2008) and has a high resolution around coastal regions and the Kuroshio path. The grid is depicted in Fig. 5a, with total node number of 127,914 and cell number of 249,294. The Kuroshio path has a high resolution of approximately 3 km, and the Changjiang coast is gridded at a resolution of approximately 1–3 km (Fig. 5a). The small gap in the middle Japan is designed to increase the model stability near the exit of Kuroshio Current. The original ECS-FVCOM described by Chen et al. (2008) is configured using modified bathymetry with 800 m cutting (bathymetry data were cut to 800 m when the water depth exceeded 800 m) and without tidal forcing along the open boundary. Only the freshwater discharge and ocean circulation were considered. Several updates were conducted in the present study to improve ECS-FVCOM, including the addition of (1) realistic ocean floor topography without depth cutting (as in Fig. 1) and (2) more general terrain-following s-coordinates with 40 vertical layers. The sea surface and bottom are discretized with five 2-m-thickness layers, and the uniform vertical sigma layers are specified in the middle region. This vertical configuration is adapted to consider the

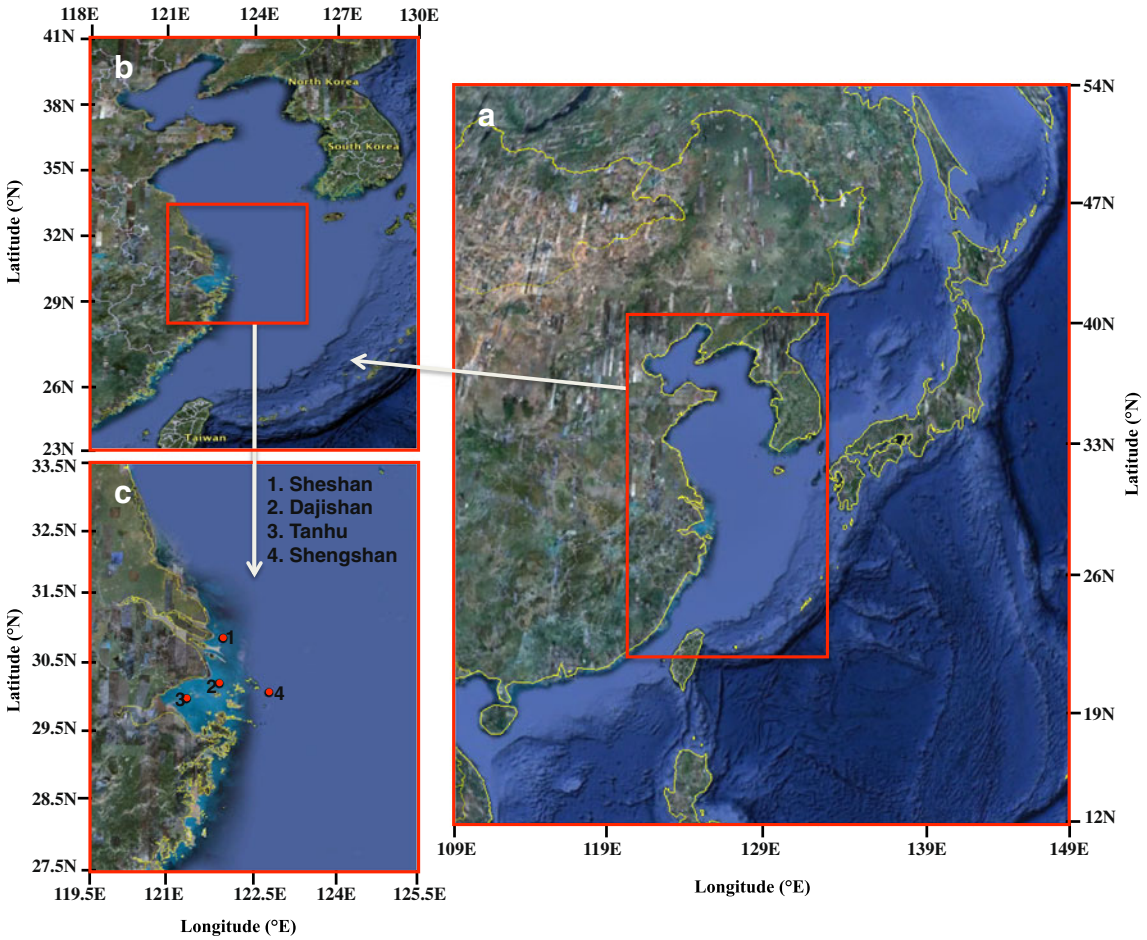

Fig. 4 Three geographic domains of the WRF model, including a basin-scale domain with an 81-km resolution (*right*), a shelf-scale domain with a 27-km resolution (*left upper*), and a region-scale domain with a 9-km resolution (*left lower*). The *four red circles* in domain 3 indicate the four meteorological stations in the Changjiang Estuary: Sheshan, Dajishan, Tanhu, and Shengshan

surface and bottom thin layers to reveal the detailed dynamics within these thin boundary layers. Two-minute time step for internal mode is used, and ratio of internal and external time step is 10. The following configurations for the open boundary and initial field are applied as follows:

1. Initial field is interpolated from daily HYCOM+NCODA Global 1/12° Analysis data (GLBa0.08).
2. Variable volume transports along the open boundary are also retrieved from HYCOM+NCODA Global 1/12° Analysis data (GLBa0.08).
3. Eight major tide harmonic constituents, M_2, S_2, K_2, N_2, K_1, O_1, P_1, and Q_1, are added along the open boundary, which is retrieved from TPXO 7.2 Global Tidal Solution (Egbert and Erofeeva 2002).

Since the HYCOM data do not contain astronomical component, the nudging algorithm to combine the HYCOM's ocean transport and astronomical tide along the boundary is described as follows:

$$\begin{aligned} U &= U_{\mathrm{H}} + U_{\mathrm{T}} \\ V &= V_{\mathrm{H}} + V_{\mathrm{T}} \\ \zeta &= \mathrm{SSH} + \zeta_{\mathrm{T}} \\ S &= S_{\mathrm{H}} \\ T &= T_{\mathrm{H}} \end{aligned} \tag{13}$$

U_{H}, V_{H}, SSH, S_{H}, and T_{H} are interpolated eastward velocity, northward velocity, sea surface height, salinity, and temperature from HYCOM+NCODA. U_{T}, V_{T}, and ζ_{T} are tidal components of velocities and sea surface elevation, which are predicted by T_tide Matlab package with harmonic constants of TPXO7.2 data.

2.5 Changjiang coastal FVCOM

The high-resolution Changjiang Estuary FVCOM model (CE-FVCOM) is configured along the nesting open boundary (blue lines in Fig. 5b), where the shelf circulation can be introduced into the inner shelf of Changjiang Estuary. The model guarantees local high-resolution discretization and provides accurate geometric fitting for both irregular coastlines and coastlines,

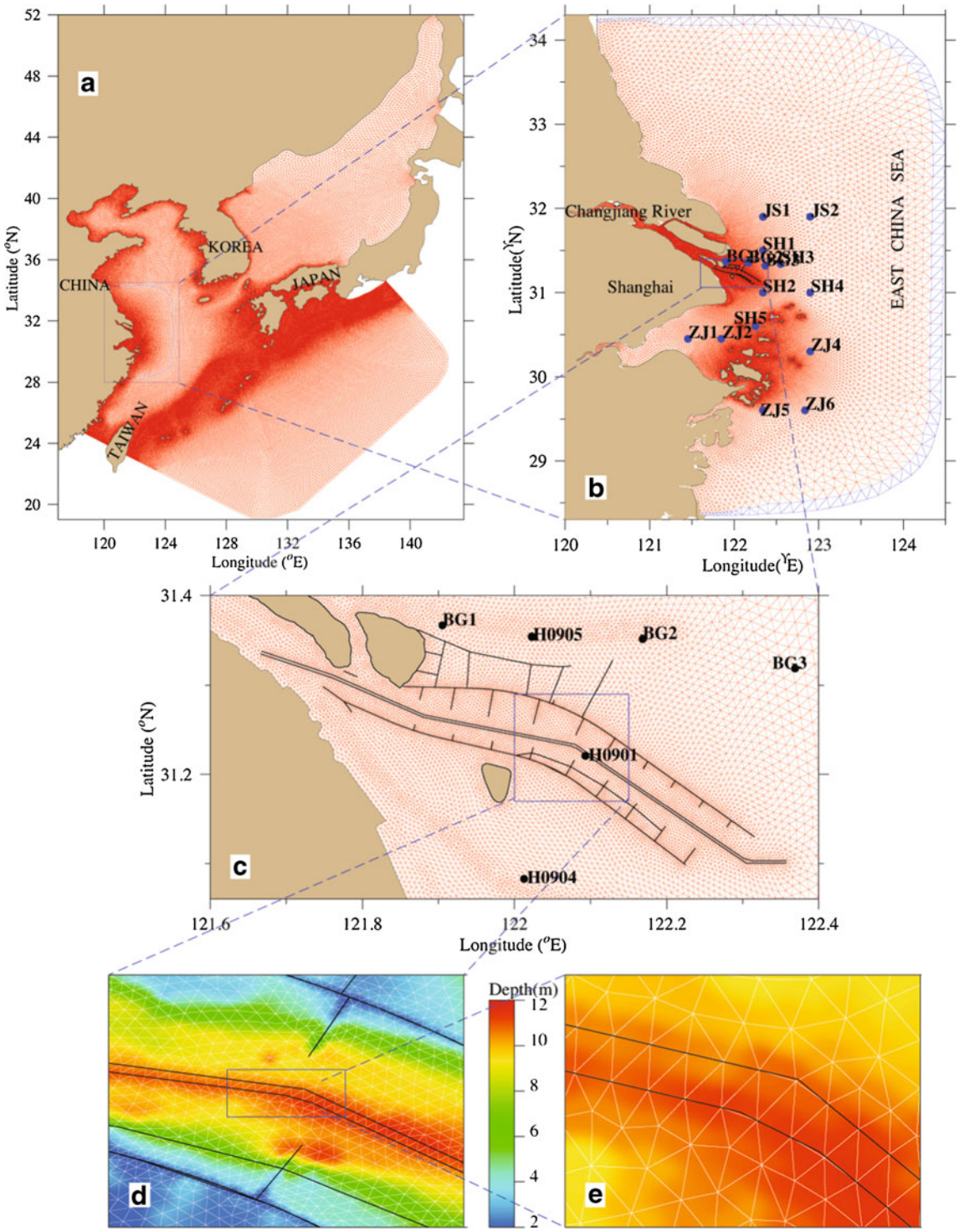

Fig. 5 High-resolution triangle grids for the East China Sea shelf (**a**), Changjiang Estuary and its adjacent regions (**b**), and the Deep Waterway Project region (**c**). Enlarged views include the middle part of the North Passage, where there are dikes and groynes (**d**) and the shipping channel region (**e**). The blue grid in **b** shows the common grid boundary for nesting between ECS-FVCOM and CE-FVCOM. The *blue dots* in **b** and *black dots* in **c** indicate the observation stations for validations

especially for the coastal engineering construction projects around the deep waterway region. The resolution is up to 500 m in the river mouth and varies from 1 to 5 km around the inner shelf. A daily freshwater discharge is added in the upstream regions of the Changjiang River and Qiantang River (source: Bureau of Hydrology, Changjiang Water Resources

Commission, www.cjh.com.cn). A total of 40 vertical layers as same as ECS-FVCOM are specified within the vertical water column, which could guarantee the mass and momentum conservation from ECS-FVCOM to CE-FVCOM through nesting boundary. The 80-m depth is transient threshold between 40 *s*-coordinate layers (five upper and bottom 2-m-thickness layers specified) and 40 uniform sigma layers. Since the bathymetry of Changjiang Estuary is mostly shallower than 80 m (Fig. 1), the CE-FVCOM is mainly discretized as 40 uniform sigma layers in vertical column. The common grid nesting method, which is shown as the blue triangle cell in Fig. 5b, is applied between ECS-FVCOM and CE-FVCOM to guarantee the conservation of mass and momentum during domain nesting calculation. Along the nesting boundary, the bathymetry is not deeper than 80 m, so all vertical *s*-coordinates in ECS-FVCOM and CE-FVCOM are all turned into uniform sigma layers, and the vertical discretizations between two domains along this boundary are identical.

2.6 Deep waterway FVCOM

An unstructured grid FVCOM has been applied to study the hydrodynamics around the Deep Waterway Project (DWP) within the North Passage, considering a realistic engineering configuration. The submerged and exposed constructions are all included in the high-resolution deep waterway FVCOM (DW-FVCOM). The DW-FVCOM has resolution of approximately 200–250 m around the DWP region, especially along the shipping channel (Fig. 5c). DW-FVCOM has provided accurate geometric fitting for dikes and groynes (Fig. 5d), and the shipping channel has also been realistically resolved with a 200-m resolution unstructured grid (Fig. 5e).

DW-FVCOM is also specified with 40 vertical layers to be nested from CE-FVCOM, and it is flexible to include different project configurations from a non-project situation to the phase III project during the last decade. These dikes and groynes are constructed ~30 cm above the mean sea level, which means that they are submerged during high tide and exposed during low tide. There is a typical two-layer structure in the vertical column near the constructions during high tide. To capture the physics around dikes/groynes accurately, the water transport process below and above the structures must be accurately resolved. Therefore, the dike–groyne treatment algorithm (Ge et al. 2012) is implemented in DW-FVCOM to reveal the two-layer dynamics.

These ECS-FVCOM, CE-FVCOM, and DW-FVCOM are exchanged through the common grid nesting method, which is used to significantly increase the computational efficiency. The ECS mesh features 249,294 cells and 127,914 nodes with a horizontal resolution of 2.0–15 km, while the local Changjiang Estuary mesh features about 95,496 cells and 50,735 nodes with the finest resolution of about 500 m, and the deep waterway mesh features 24,583 cells and 13,110 nodes with resolution of ~200 m along the shipping channel. The time step of internal mode is 2 min for the regional ECS domain, 40 s for the Changjiang Estuary, and 10 s for the local North Passage domain. The time step used for the three subdomains must be multiple of each other in order to avoid interpolation in time to reduce the conservation error when nesting. And the ratios of internal and external time step are all 10 for three models. This nesting approach improved the overall computational efficiency by a factor of 10. FVCOM-SWAVE is all activated in three models to predict the wave conditions from open oceans to local channels.

3 Validation of the model system

3.1 Surface wind

Time series data from four meteorological observation stations, Dajishan, Tanhu, Sheshan, and Shengshan (red solid points in domain 3 of Fig. 4), are selected to perform validation of the regional and local WRF model. Model–data comparisons of wind speed *u*-component and *v*-component at these four stations during May of 2006 are given in Fig. 6. It shows good agreement between the observations and the simulation. Additionally, it has successfully revealed the wind patterns during both strong and weak situations. The overall RMS error of these four stations is 2.28 m/s, indicating that this weather model has the capability of providing reasonable surface forcing over the shelf of the East China Sea and Changjiang Estuary.

3.2 Tide

ECS-FVCOM has been validated using observation tidal harmonic constituents of gauge data. A total of 99 gauge stations are used to make these comparisons, and the locations of these gauges are shown as red points in the left panel of Fig. 1. The harmonic constants of model simulation are analyzed with T_tide Matlab package (Pawlowicz et al. 2002). Model–data comparison for principle M_2 harmonic constants (amplitude and phase) is shown in Fig.7a, b. The correlation coefficients for amplitude and phase reach 0.95 and 0.98, and the standard derivations are 8.60 cm for amplitude and 9.44° for phase, respectively. This comparison shows that ECS-FVCOM produces good astronomical tide simulations. The distributions of the co-amplitude and co-phase over the East China Sea are shown in Fig. 8 and agree well with observations for the major tide constituents of M_2, S_2, K_1, and O_1 (Atlas of Bohai Sea Yellow Sea and East China Sea 1994).

The Changjiang FVCOM is also validated with observation data of M_2's amplitude and phase at the coastal gauge stations (red points in Fig. 1b). CE-FVCOM has exhibited

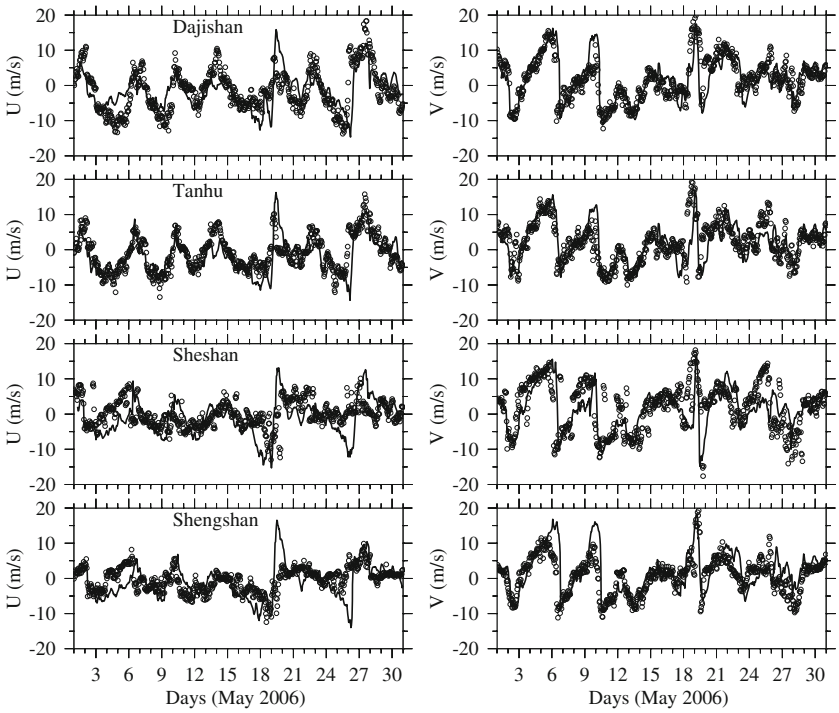

Fig. 6 Model–data comparisons for the U-component and V-component of 10-m-height wind at the Dajishan, Tanhu, Sheshan, and Shengshan meteorological stations

very good agreement with the observed harmonic constants (Fig.7c, d), showing correlation coefficients reach 0.95 and 0.99 for amplitude and phase, respectively. Their standard errors are 8.4 cm and 8.65°. These error statistics show that the CE-FVCOM has precisely revealed the dominant dynamics around the Changjiang Estuary.

Additionally, validation with observed data of hourly elevation series and their subtidal component are conducted at three stations in the Changjiang Estuary. These three stations, Baozhen, Chongxi, and Nanmen, are under the influence of river runoff, wind, and tide. The PL64TAP Matlab program is used to determine their subtide components with half amplitude

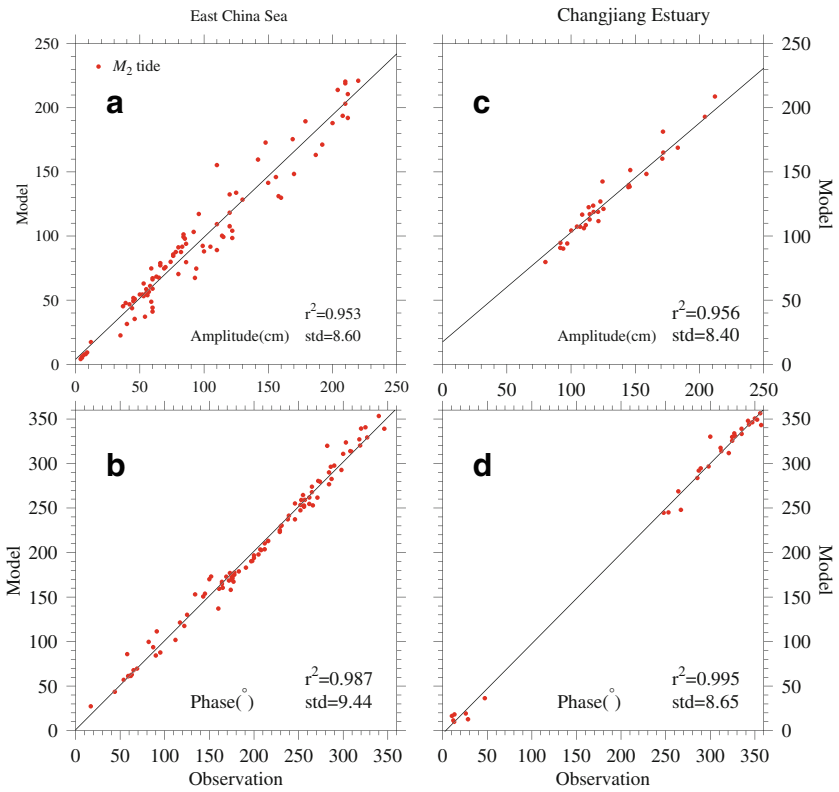

Fig. 7 Comparisons between modeled and observed tidal harmonic constants (amplitudes and phases) of the principal tidal constituent M_2 for East China Sea (*left column*) and Changjiang Estuary (*right column*)

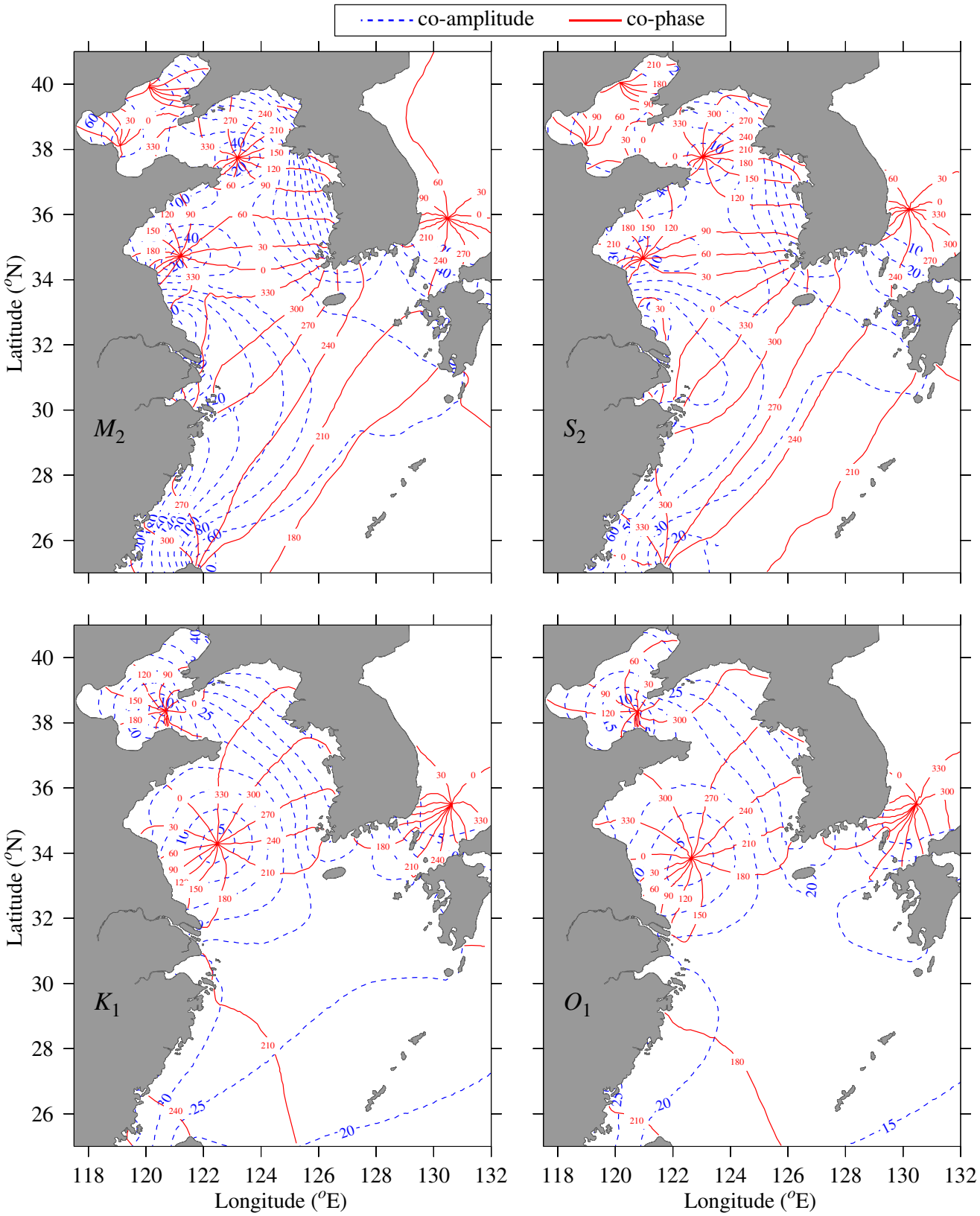

Fig. 8 Distributions of the co-amplitude (*blue dashed lines*) and co-phase (*red solid lines*) of the M_2, S_2, K_1, and O_1 tide constituents around the East China Sea, Yellow Sea, and Bohai Sea

period of 33 h and half power period of 38 h (Beardsley 2005). Figure 9 shows the model–data comparison, which indicates that the model has made good prediction for surface elevation with overall RMS error of 19 cm. Its subtidal variation is also well reproduced, which is mainly caused by varying upstream runoff and local atmospheric wind forcing.

3.3 Current

The model was validated using the field survey data collected around the mouth of the CE in the summer of 2010. One cruise was made from neap to spring tides (Aug 18–19 for neap tide, Aug 25–26 for spring tide), and each station was observed for 26 h to cover one tidal cycle. Anchoring sites are shown as filled dots in Fig. 5c. BG1, BG2, and BG3 were the stations in the North Channel of the Changjiang River mouth.

In these field measurements, the current profiles were recorded using the Acoustic Doppler Current Profiler (ADCP) from the RD Instrument Company. The ADCP acoustic frequency is 600 KHz, with a cell size of 1.00 m and sensor depth of 1.00 m. The sampling interval was 60 s. The hourly data of velocity and direction are selected to make model–data comparison.

The model–data comparisons of BG1, BG2, and BG3 for the velocity and direction of surface, middle, and bottom layers are shown in Fig. 10. It has indicated that CE-FVCOM produced good simulations of current velocity and direction around the estuary. This model has revealed the current structures and their variations associated with tide oscillations and Changjiang River discharge in the river mouth. In the upper stream BG1, the river discharge is dominant against the tide, and the current direction mainly flows eastward (~120°) during neap tide cycle, even at flood maximum, and it gradually has westward pattern during the flood tide with the growing of astronomical tide from neap to spring tide cycle. The model system also correctly reveals the variation of current at BG2 and BG3. Although there is overestimation at lower column of BG2 during neap tide, main characteristics of current from upper and lower estuary

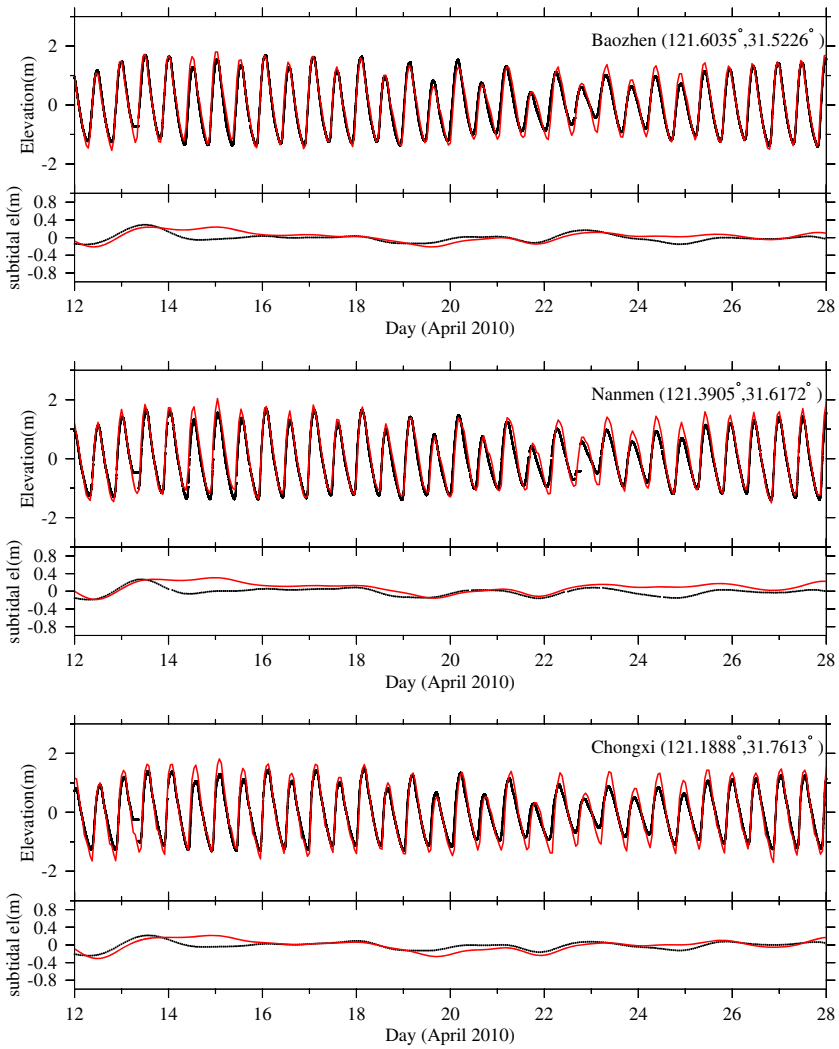

Fig. 9 Model–data comparisons between modeled (*red lines*) and observed (*black dots*) elevation at Baozhen, Nanmen, and Chongxi stations. The subtidal components are also included

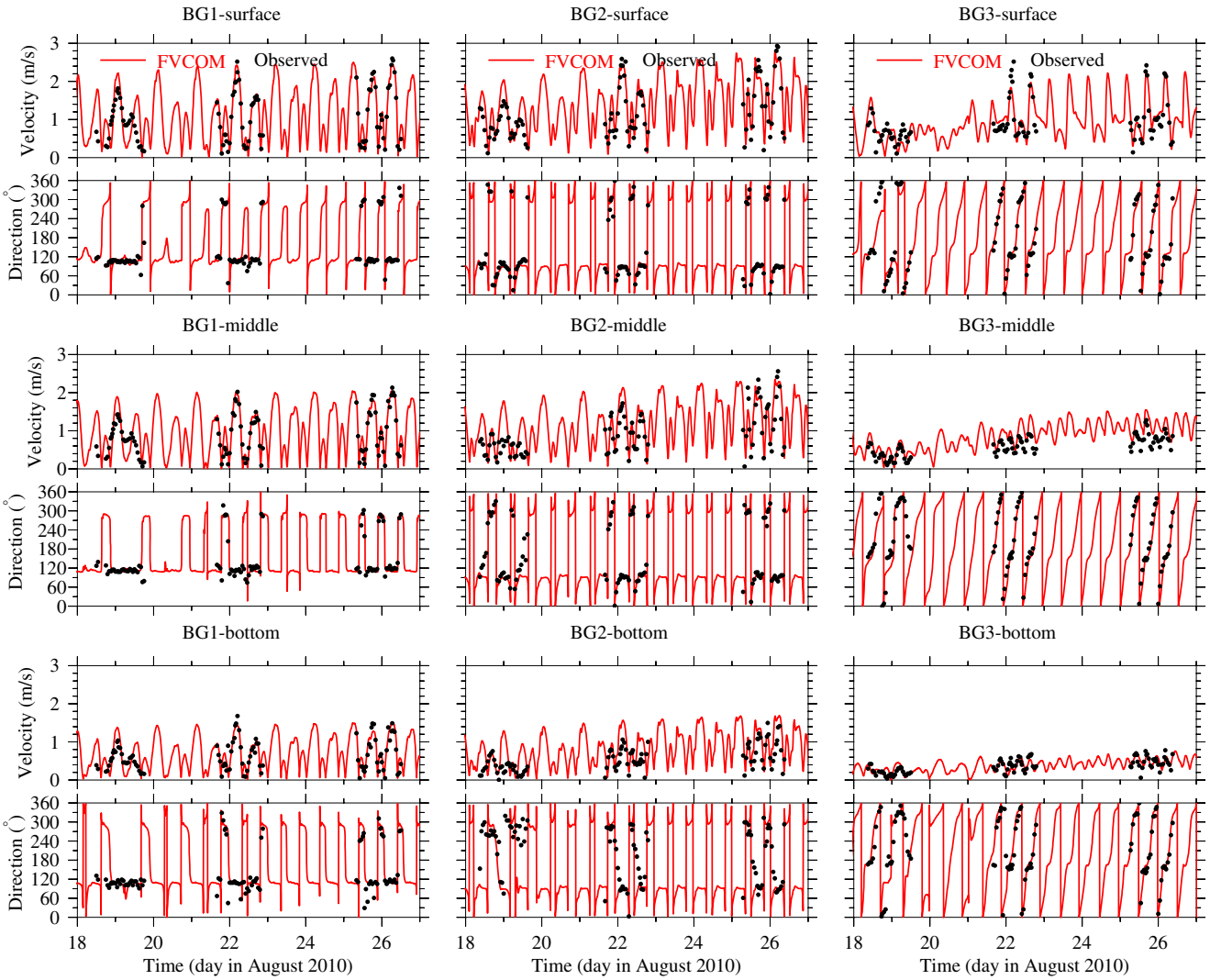

Fig. 10 Model–data comparisons of velocity and direction at the surface, middle, and bottom layers at BG1, BG2, and BG3 around the Changjiang Estuary. The *red lines* indicate the modeling results and the *black points* the observation data

are well captured. The complex hydrodynamics around the BG3 during whole spring-neap cycle is well simulated under the joint influences of river runoff and seawater. And the vertical structures and its variations of velocity and direction are reasonably simulated.

3.4 Salinity

The salinity data used for validation also come from the summer observation as current validation in Section 3.3. Vertical profiles of turbidity, temperature, and salinity were measured using the Optical Backscatter Sensor (OBS)-3A from the D&A Instrument Company. The water columns were profiled hourly during the observation.

Figure 11 shows the comparisons of the time-series salinity comparisons at stations SH4, SH5, ZJ1, and ZJ2 during spring tide cycle and SH1, SH2, SH5, and ZJ2 during neap tide cycle. The model captured the temporal variation of the surface observed salinity at most stations. CE-FVCOM slightly overestimated the variation range over the tidal cycle at SH2 where is a front zone between low-salinity water from river and saltwater from shelf. The overall RMS error for these stations is 2.07 psu. The error range is mainly affected by the overestimation at SH2. The RMS errors for other stations are mostly less than 1.5 psu. The model–data comparison of salinity shows that the model system has captured the main characteristics and its spatial and temporal variations of low-salinity water in the Changjiang Estuary and inner shelf of East China Sea.

3.5 Wave

Surface wave process is also validated using observation data from a buoy station (123.59° E, 29.29° N) during two

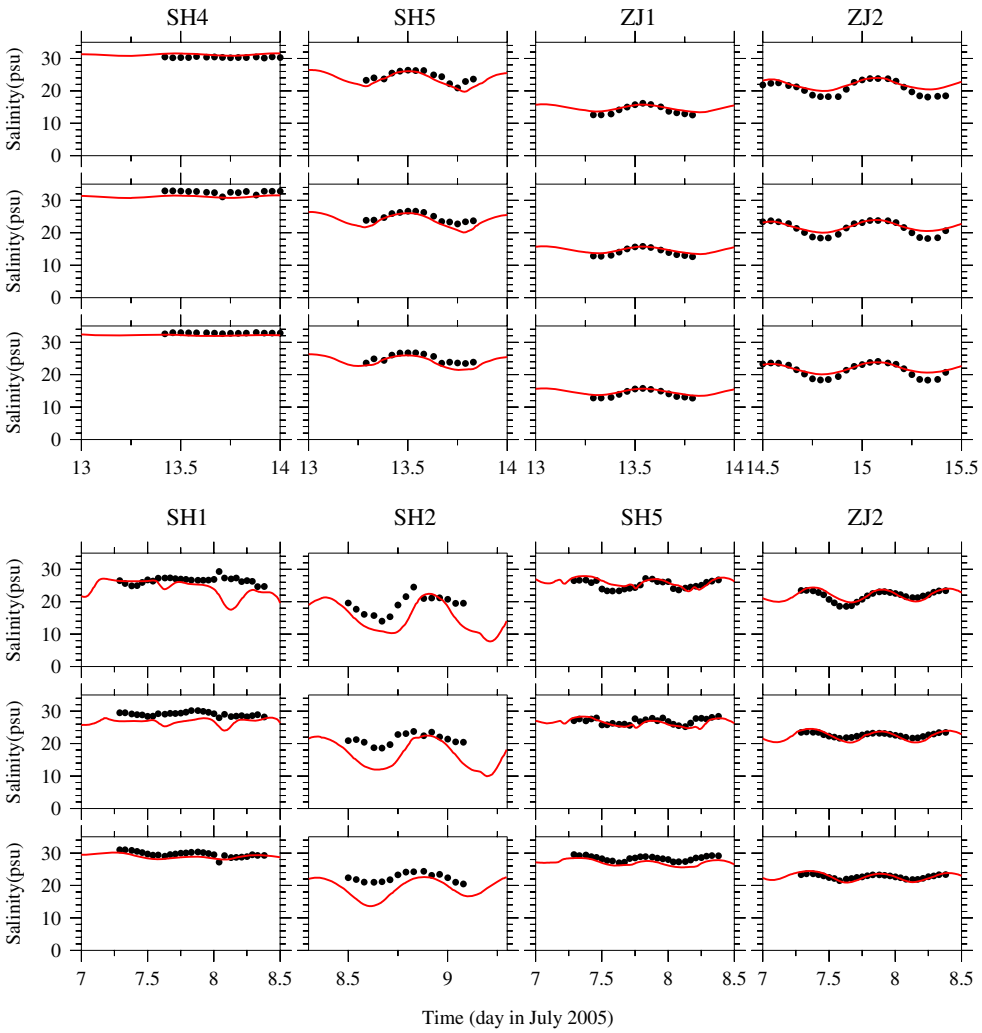

Fig. 11 Model–data comparisons for salinities in the surface (*upper row*), middle (*middle row*), and bottom (*lower row*) layers at SH4, SH5, ZJ1, and ZJ2 during the spring tide cycle and SH1, SH2, SH5, and ZJ2 during the neap tide cycle. The *red lines* indicate the modeling results and the *black points* the observation data

continuous typhoon attacks (Sinlaku and Rusa) in the summer of 2002. The time-series wave data are acquired by Directional Waverider DWR-MK2 attached to the 2-m-radius floating buoy. The FVCOM-SWAVE is activated under the forcing of typhoon wave simulation by WRF in this model system. The high-resolution ECS-FVCOM exhibits good agreement with the observed data regarding the significant wave height (H_s) and relative wave period (T_p), which are shown in Fig. 12. The RMS errors for 10-m-height wind speed and significant wave height are 1.3 m/s and 0.54 m, respectively. The ECS-FVCOM has successfully revealed the strong waves that occur because of two continuous typhoon impacts, which reach maximum wind speed of 21 m/s and significant wave height of 8.0 m.

4 Applications of the model system

The model system has been applied to various studies addressing multi-scale dynamics, such as those of the Changjiang low-salinity plume detachment (Chen et al. 2008). In this paper, two additional examples of applications over the Changjiang Estuary using integrated modeling are presented. One example involves simulation of seasonal Changjiang diluted water spreading, and another reveals the saltwater intrusion pattern within the North Passage due to the construction of dikes and groynes.

4.1 Seasonal spreading of Changjiang diluted water

Under the influence of the Changjiang River, providing an abundant freshwater supply, the dynamics of the Changjiang Estuary are strongly controlled by low-salinity, diluted water, which results in a significant two-layer structure consisting of an upper low-salinity plume and lower saltwater layer (Hu et al. 2002; Zhu et al. 2004; Chen et al. 2008). Because of the seasonal fluctuation of the freshwater discharge from the CR, the spreading of the diluted water exhibits significant seasonal variation near the river mouth. The spreading and mixing of the diluted water are also strongly influenced by multiple dynamics,

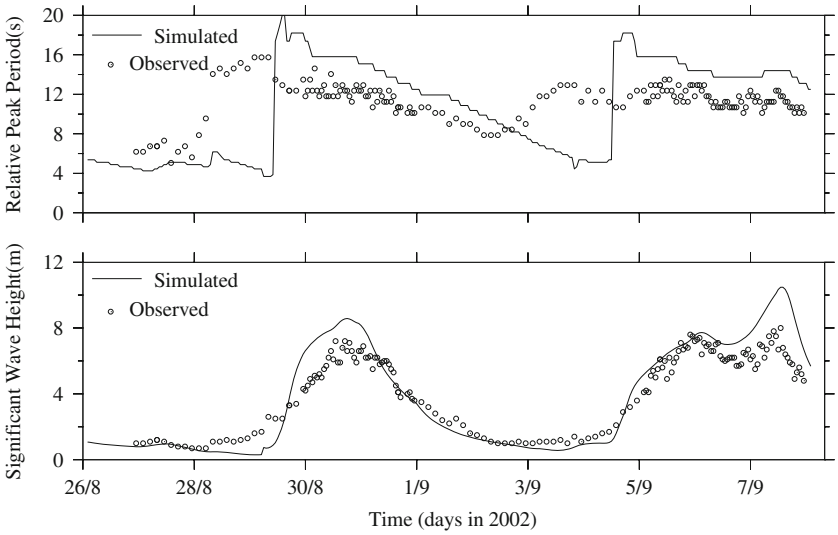

Fig. 12 Model–data comparisons of buoy wave data, including the wind velocity (*upper*) and significant wave height (*lower*). *Solid lines* indicate the modeling results and *black circles* the observation data

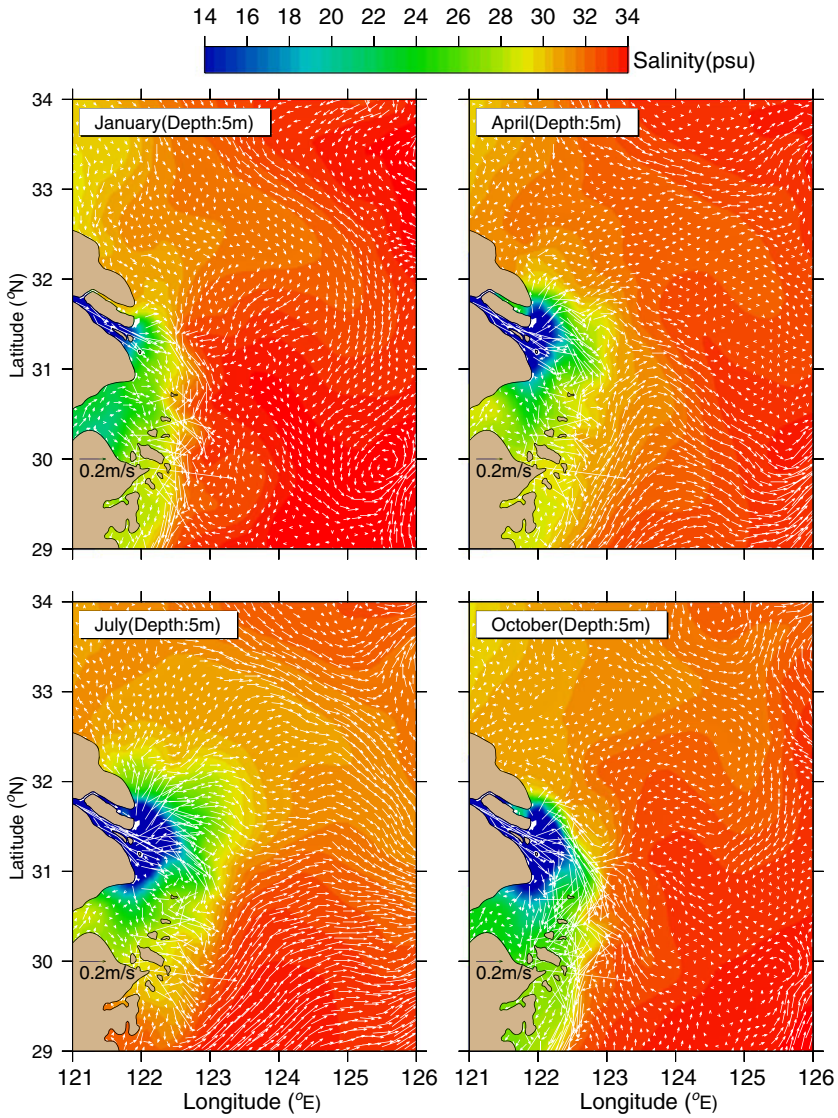

Fig. 13 Monthly averaged salinity distributions at a depth of 5 m in January, April, July, and October around Changjiang Estuary and its adjacent regions under climatological seasonal forcings

including seasonal monsoon winds, semidiurnal tidal oscillations, remote ambient flow, and submerged trenches.

Following the validations of the salinity processes occurring in and out of the estuary, the multi-scale model system is applied to simulate the seasonal variations of the low-salinity diluted water under these multiple effects. The model is initialized using 10-km resolution 3-D seasonal climatology hydrographic fields and a specified water transport of the Kuroshio, Taiwan Warm Current, and other ocean volume transport at the open boundary. The hydrographic fields were constructed using 10-km box averaging of historical water temperature and salinity data collected in this region over the last 40 years. The model was first spun up with the seasonal climatology hydrographic fields and fixed inflow and outflow transports for 30 model days. Since the Kuroshio and shelf circulation reached quasi-steady state after 30 model days, the seasonal river discharge was started on model day 31 by adding a freshwater discharge climatological value at the upstream end grid of the Changjiang domain. The Changjiang plume was established by model day 60. The final results are model days 61–90 averaged.

The results for January, April, July, and October are selected to show the typical distributions of near-surface salinity and residual currents in winter, spring, summer, and autumn season, respectively (Fig. 13). The spatial coverage changes according to the seasonal river discharge, such that the winter season shows the smallest diluted water plume and summer presents the greatest diluted water extension. In the winter, the diluted water mainly flows southward off the coastline under the influence of the southeastern monsoon and low CR discharge rate (~10,000 m^3/s). Additionally, the northward Taiwan Warm Current is not notable in winter, which could have contributed to the northward flow of the diluted water. With increasing freshwater discharge rates (~24,000 m^3/s) and onshore winds, the diluted water shifted, showing a northward extension during spring, and the river mouth was then dominated by relatively

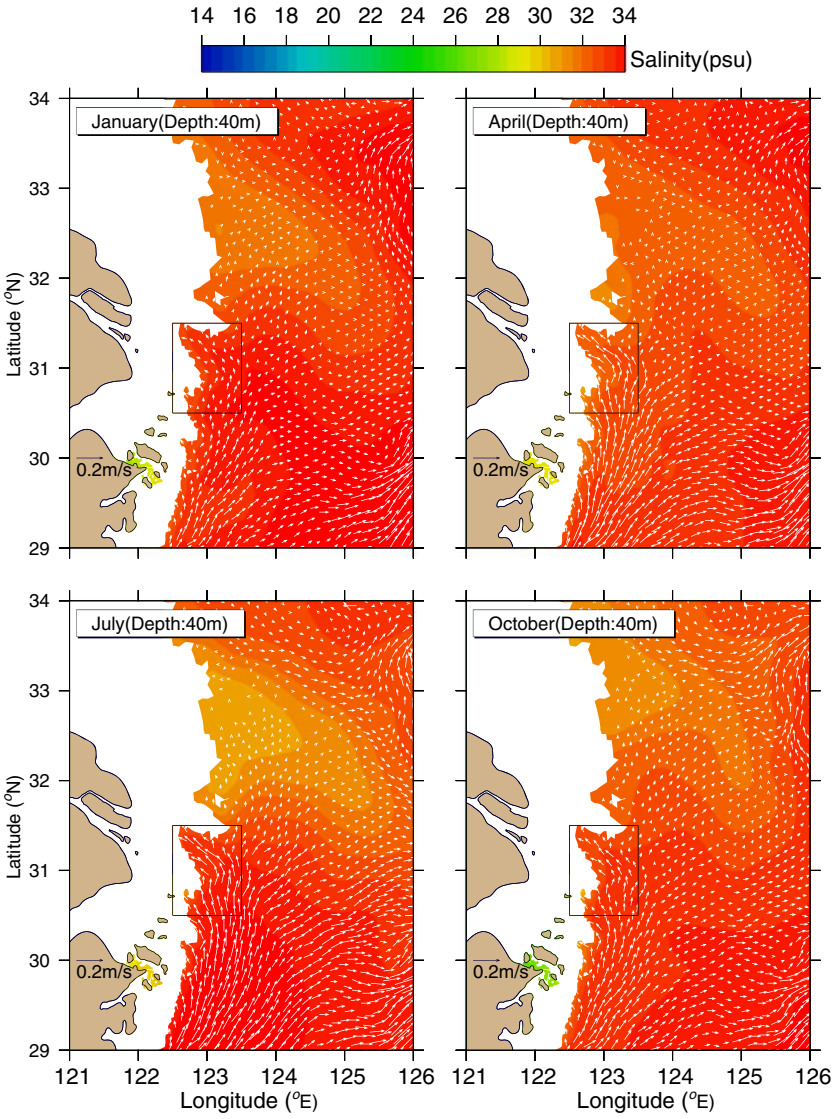

Fig. 14 Monthly averaged salinity distributions at a depth of 40 m in January, April, July, and October around Changjiang Estuary and its adjacent regions under climatological seasonal forcings

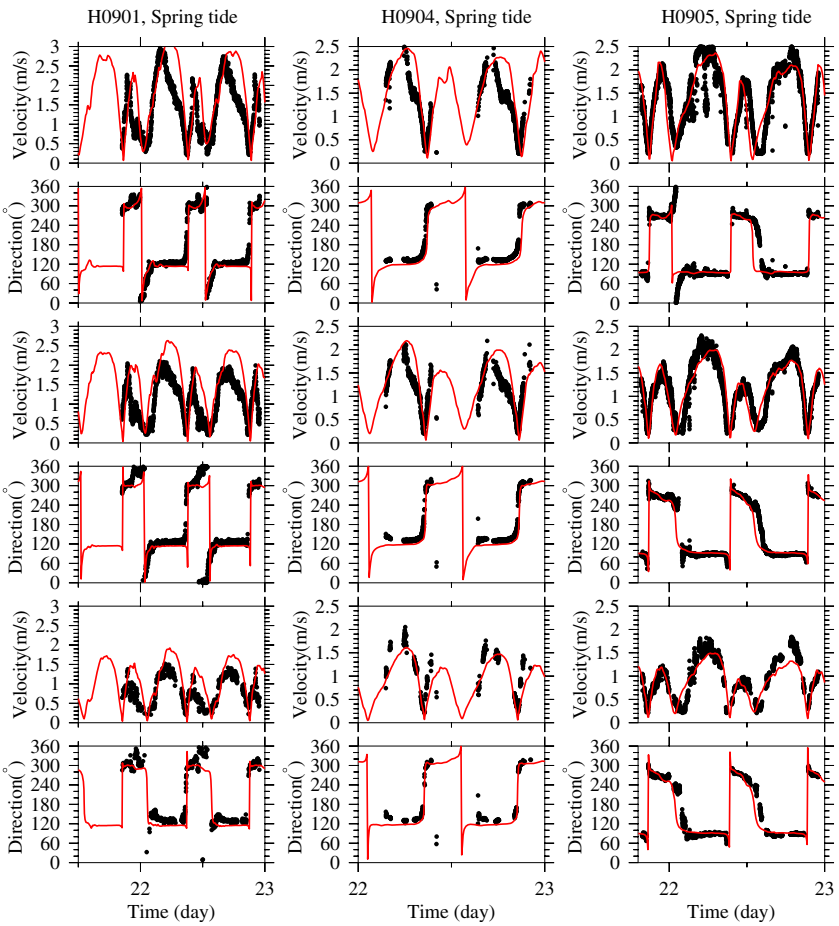

Fig. 15 Model–data comparisons of the surface velocity (*first row*), surface direction (*second row*), middle layer velocity (*third row*) and direction (*fourth row*), and bottom velocity (*fifth row*) and direction (*sixth row*) during the spring tide cycle in August 2009 at H0901, H0904, and H0905 around the North Passage. The *red lines* indicate the modeling results and the *black points* the observation data

low-salinity water. This phenomenon is strongly intensified during summer, as the monsoon wind shifts to blowing in a northwest direction, and the strength of Taiwan Warm Current is increased in this season. The low-salinity plume shows a northeastward trend, spreading under the strongest influence of the freshwater discharge (>50,000 m^3/s) and becomes weaker in autumn because the freshwater discharge (~32,000 m^3/s) decreased and the wind direction changed. The results obtained for the surface patterns agree well with the long-term average distribution presented in ATLAS for the Bohai Sea, Yellow Sea, and East China Sea (1994).

The interaction between the freshwater impact of CR and the onshore ocean circulation produces a typical two-layer system consisting of an upper low-salinity diluted water layer and a lower salty ocean water layer, which is more obvious during summer. There are significant bottom onshore ocean circulation intrusions off the Changjiang Estuary (black-box region in Fig. 14). The intrusion intensity is relatively weaker in winter and is stronger in summer. The high-salinity water mainly flows along the offshore submerged trench around the 40-m isobath. This characteristic is in accord with previous observations of upwelling made in investigations performed off the Changjiang Estuary (Zhu et al. 2004). This simulation indicates not only that the salinity distributions show vertical

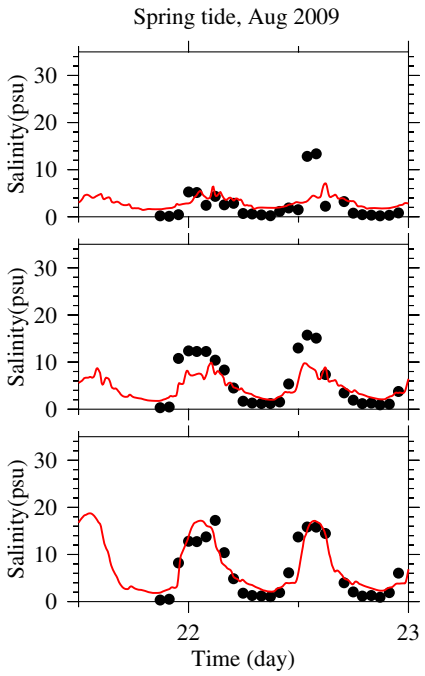

Fig. 16 Model–data comparisons for salinities in surface (*upper row*), middle (*middle row*), and bottom (*lower row*) layers at station H0901 during the spring tide in August 2009

stratification in the offshore region but also that the residual structures are opposite, with the offshore direction occurring in the near-surface layer and onshore direction associated with the near-bottom layer.

4.2 Summer saltwater intrusion and flow structures within the north passage

The multi-scale model system is applied to study the salinity distributions under the realistic conditions, compared with observational data around the North Passage. Three mooring sites are located in the South Passage (H0904), the North Passage (H0901), and the North Channel (H0905) (Fig. 5c). The RDI ADCP workhorse (600 K) monitors were applied to observe the current profiles at these stations, and the surveying is also specified with 26 h in spring and neap tide cycles as observation in Section 3.3. The ADCP sensor depth is 0.5 m, and cell size is 0.5 m. And the salinity of water column is profiled with OBS-3A.

The model system is initialized with climatological hydrodynamic filed in August and spin up for 30 days. The daily-observed freshwater discharge rate is added in the upstream end of Changjiang River, and the model running for another 30 days to let the low-salinity plume is formed. The model days 61–90 covers the observation time. And the results of final 30 days are used to make model–data comparison and analysis.

Model–data comparisons of velocity and current at surface, middle, and bottom layers for these sites are presented in Fig. 15, showing that DW-FVCOM has successfully revealed the hydrodynamic characteristics of currents and their variations associated with tide oscillations and freshwater discharge. The observation and DW-FVCOM data show that there was a strong tidal current along the shipping channel (near H0901), with the maximum velocity ~3.0 m/s. The averaged RMS errors at these three stations for velocity and direction are 33 cm/s and 27°, respectively.

Furthermore, the DW-FVCOM and observation data have revealed the strong vertical stratification during spring tide cycle at the H0901 site (Fig. 16), which indicates that low salinities dominated the upper layer (mostly less than 10 psu), while high-salinity water controls the bottom layer (approximately 20 psu at maximum flood). DW-FVCOM shows a typical two-layer structure near the observation site. The time series variation related to the astronomical tide shows that there is significant saltwater intrusion during the

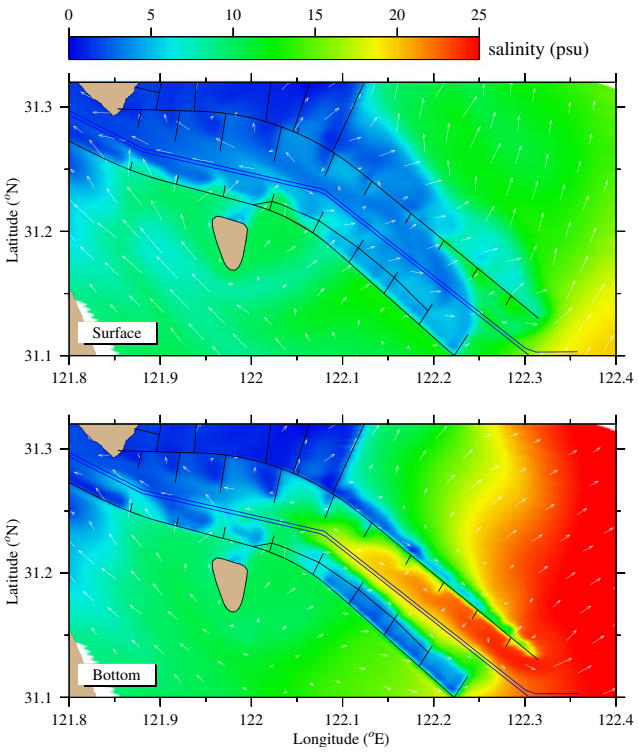

Fig. 17 Model-predicted salinity distributions in the surface and bottom layers during the maximum flood tide around the North Passage. The *black lines* indicate constructions of dikes and groynes

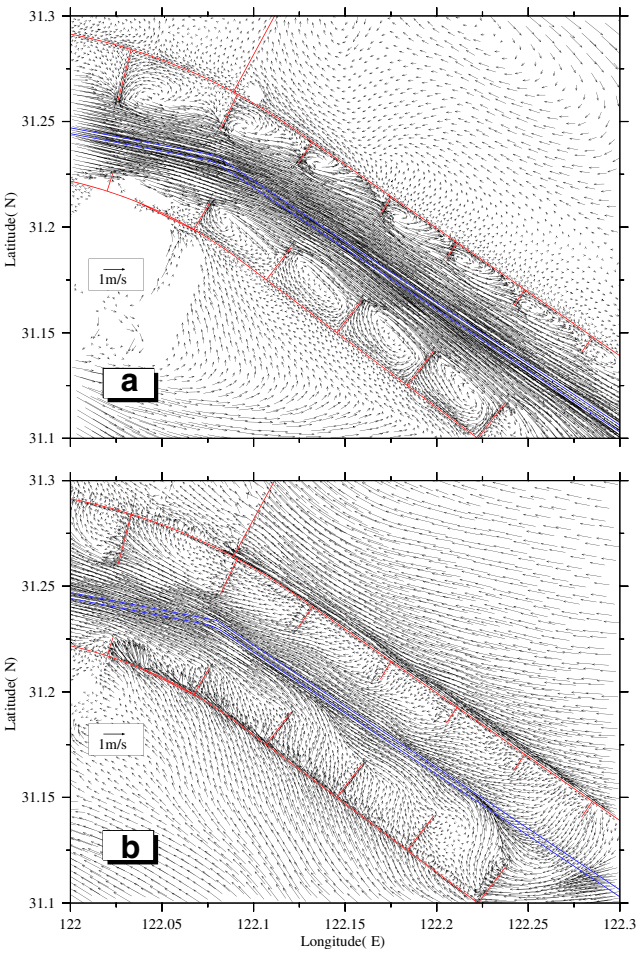

Fig. 18 Surface current distributions at maximum ebb (**a**) and maximum flood tide (**b**) around the North Passage

flood tide cycle when the high-salinity seawater was moving onshore into the North Passage.

The salinity distribution in the surface and bottom layers during the maximum flood tide is given in Fig. 17, which indicates that a significant two-layer system dominates the area near the mouth due to the gravitational salt wedge during summer of a high discharge rate 40,000~45,000 m^3/s. It shows that low salinity water floats on the surface (upper panel of Fig. 17), while relatively high salinity water sinks in the lower column, and the bottom saltwater is transported onshore into the North Passage. The high-salinity bottom water is constrained by the dikes and groynes and thus moves upstream, with a maximum extension to the middle region of the shipping channel (lower panel of Fig. 17). Because flocculation mainly occurs within a salinity range of 5–10 psu (Krone 1962), saltwater with a salinity of 5–10 psu has covered the middle region, where significant deposition occurs and the major dredging operations are carried out. The bottom salinity intrusion into the North Passage during summer might be a potential factor to influence sediment deposition and back siltation around the shipping channel.

Because the heights of the dikes and groynes correspond to the mean sea level, they will be exposed during low ebb tide. These constructions act as solid blocking boundaries, and therefore, the current structure within the North Passage at maximum ebb is characterized by strong flows along the main channel region and small eddies in groyne-blocked areas (Fig. 18a). A strong current flows along the shipping channel and was enhanced after the dikes and groynes were built (Ge et al. 2012). The dimensions of eddies depend on the length and distance between groynes. The eddies constrained within the south groyne-blocked regions are much larger than those within north regions of short groynes. When the water level exceeds the tops of the dikes and groynes during high flood tides, there are significant cross-dike currents from the Jiuduansha Shoal to the North Passage, which decreases the strength of the eddies (Fig. 18b).

5 Conclusion

An unstructured grid high-resolution model system has been established with the aim at resolving the multi-scale coastal ocean dynamic processes around the East China Sea shelf and the Changjiang Estuary as well as its adjacent coastal regions. Three FVCOM-based three-level nesting hydrodynamic models have been built to accurately reveal the dynamics around the East China Sea, Changjiang Estuary, and local deep waterway region. Several internal modules are essential for the setup and configuration of the model, including a wave–current interaction module, a dike–groyne treatment module to deal with the ocean engineering structures of dikes in the deep waterway, and a common-grid nesting module to guarantee the conservational transferring of momentum and mass along the nesting boundary. It has the capability of revealing detailed structures of hydrodynamics of varying scale. This model system has been validated with various observation data and shown promising results with high predicting precision. The capability of the model system is demonstrated with the simulations of the shelf-scale diluted water propagation in the inner shelf of ECS. The variation and distribution of onshore saltwater intrusion along the North Passage during summertime are captured. The maximum intrusion front could reach the middle region of North Passage, where the channel siltation significantly occurred. It could be partially affected by the salinity-induced flocculation process.

This model system provides a unique tool for studying the multi-scale dynamics around the East China Sea and Changjiang Estuary and has already been validated and applied in the various studies. It could represent potential framework for developing the China regional forecast system after more validation against observation data and tested with realistic forecasting events.

However, sediment and morphology process, one of the dominant dynamics in the Changjiang Estuary, has not been fully validated under the strong current and waves. The future work is to improve the sediment module to capture the distribution and variation of suspended- and bed-load sediment and to couple the wave–current–sediment interaction in the model system.

Although the model system is used around the East China Sea, methods used in the development of this FVCOM-based model system are generalized and could be applied to other shelf regions and coastal areas to produce high-resolution multi-scale and multi-dynamics simulations in kind.

Acknowledgments Jianzhong Ge and Pingxing Ding are supported by the Fund from Creative Research Groups of NSFC (no. 41021064), Public Service Program of State Ocean Administration (contract no. 201205017-2), and the SKELC independent fund (2011RCDW03). Song Hu is supported by the Program of Science and Technology Commission of Shanghai Municipality (09320503700). Authors would like to express their appreciations to three anonymous reviewers, who provided very helpful suggestions to improve the manuscript.

References

Atlas of Bohai Sea Yellow Sea and East China Sea (1994) China Ocean, Beijing, p 46

Barth A, Alvera-Azcárate A, Weisberg RH (2008) Benefit of nesting a regional model into a large-scale ocean model instead of climatology. Application to the West Florida Shelf. Cont Shelf Res 28(4–5):561–573. doi:10.1016/j.csr.2007.11.004

Beardsley R (2005) Vector correlation, complex correlation, and other tools from Bob Beardsley (WHOI). http://woodshole.er.usgs.gov/operations/sea-mat/bobstuff-html/index.html

Beardsley R, Limeburner R, Yu H, Cannon GA (1985) Discharge of the Changjiang (Yangtze River) into the East China Sea. Cont Shelf Res 4:57–76

Beardsley R, Limeburner R, Kim K, Candela J (1992) Lagrangian flow observations in the East China, Yellow and Japan Sea. La Mer 30:297–314

Cailleau S, Fedorenko V, Barnier B, Blayo E, Debreu L (2008) Comparison of different numerical methods used to handle the open boundary of a regional ocean circulation model of the Bay of Biscay. Ocean Model 25:1–16

Chang P-H, Isobe A (2003) A numerical study on the Changjiang diluted water in the Yellow and East China Seas. J Geophys Res 108(C9):3299. doi:10.1029/2002JC001749

Chao Y, Li Z, Farrara J, Mcwilliams JC, Bellingham J, Capet X, Chavez F et al (2009) Development, implementation and evaluation of a data-assimilative ocean forecasting system off the central California coast. Deep-Sea Res II Top Stud Oceanogr 56(3–5):100–126. doi:10.1016/j.dsr2.2008.08.011

Chassignet EP, Hurlburt HE, Smedstad OM, Halliwell GR, Hogan PJ, Wallcraft AJ, Baraille R et al (2007) The HYCOM (HYbrid Coordinate Ocean Model) data assimilative system. J Mar Syst 65(1–4):60–83. doi:10.1016/j.jmarsys.2005.09.016

Chen J, Li D, Chen B, Hu F, Zhu H, Liu C (1999) The processes of dynamic sedimentation in the Changjiang Estuary. J Sea Res 41(1–2):129–140. doi:10.1016/S1385-1101 (98) 00047–1

Chen C, Liu H, Beardsley RC (2003a) An unstructured, finite-volume, three–dimensional, primitive equation ocean model: application to coastal ocean and estuaries. J Atmos Ocean Technol 20(1):159–186

Chen C, Zhu J, Beardsley RC, Franks PJS (2003b) Physical–biological sources for dense algal blooms near the Changjiang River. Geophys Res Lett 30(10):1515. doi:10.1029/2002GL016391

Chen C, Cowles G, Beardsley RC (2006a) An unstructured grid, finite-volume coastal ocean model: FVCOM user manual, 2nd edn. SMAST/UMASSD technical report 06-0602, 1–20

Chen C, Beardsley RC, Cowles G (2006b) An unstructured grid, finite-volume coastal ocean model (FVCOM) system. Special issue entitled "Advance in computational oceanography". Oceanography 19(1):78–89

Chen CH, Huang RC, Beardsley H, Liu QX, Cowles G (2007) A finite-volume numerical approach for coastal ocean circulation studies: comparisons with finite difference models. J Geophys Res 112, C03018. doi:10.1029/2006JC003485

Chen C, Xue P, Ding P, Beardsley RC, Xu Q, Mao X, Gao G, Qi J, Li C, Lin H, Cowles G, Shi M (2008) Physical mechanisms for the offshore detachment of the Chanjiang diluted water in the East China Sea. J Geophys Res 113, C02002. doi:10.1029/2006JC003994

Delcroix T, Murtugudde R (2002) Sea surface salinity changes in the East China Sea during 1997–2001: influence of the Yangtze River. J Geophys Res 107(C12):8008. doi:10.1029/2001JC000893

Egbert GD, Erofeeva SY (2002) Efficient inverse modeling of barotropic ocean tides. J Atmos Ocean Technol 19(2):183–204

Ge J, Chen C, Qi J, Ding P, Beardsley RC (2012) A dike–groyne algorithm in a terrain-following coordinate ocean model (FVCOM): development, validation and application. Ocean Model 47(C):26–40. doi:10.1016/j.ocemod.2012.01.006

Guo X, Miyazawa Y, Yamagata T (2006) The Kuroshio onshore intrusion along the shelf break of the East China Sea: the origin of the Tsushima Warm Current. J Phys Oceanogr 36(12):2205–2231

Haidvogel DB, Arango H, Budgell WP, Cornuelle BD, Curchitser E, Di Lorenzo E, Fennel K et al (2008) Ocean forecasting in terrain-following coordinates: formulation and skill assessment of the Regional Ocean Modeling System. J Comput Phys 227(7):3595–3624. doi:10.1016/j.jcp.2007.06.016

Hu F, Hu H, Gu G (2002) Studies of fronts in the Changjiang Estuary. East China Normal University Press, East China, pp 35–40, in Chinese

Hu K, Ding P, Zhu S, Kong Y (2004) Numerical simulation of typhoon waves around the waters of the Changjiang Estuary: a case study of Typhoon Rusa and Typhoon Sinlaku. Acta Oceanol Sin 26(5):23–33

Isobe A, Matsuno T (2008) Long-distance nutrient-transport process in the Changjiang river plume on the East China Sea shelf in summer. J Geophys Res Oceans 113, C04006. doi:10.1029/2007JC004248

Krone RB (1962) Flume studies on the transport of sediment in estuarine shoaling processes. Hydr. Eng. Laboratory, Univ. of Berkeley, Berkeley

Lane EM, Walters RA, Gillibrand PA, Uddstrom M (2009) Operational forecasting of sea level height using an unstructured grid ocean model. Ocean Model 28(1–3):88–96. doi:10.1016/j.ocemod.2008.11.004

Li G, Han X, Yue S, Wen G, Rongmin Y (2006) Monthly variations of water masses in the East China Seas. Cont Shelf Res 26:1954–1970

Lie H-J, Cho C-H, Lee J-H, Lee S (2003) Structure and eastward extension of the Changjiang River plume in the East China Sea. J Geophys Res 108(C3):3077. doi:10.1029/2001JC001194

Mason E, Molemaker J, Shchepetkin AF, Colas F, McWilliams JC, Sangra P (2010) Procedures for offline grid nesting in regional ocean models. Ocean Model 35:1–15. doi:10.1016/j.ocemod.2010.05.007

Mellor G (2005) Some consequences of the three-dimensional current and surface wave equations. J Phys Oceanogr 35:2291–2298

Michalakes J, Dudhia J, Gill D, Henderson T, Klemp J, Skamarock W, Wang W (2004) The weather research and forecast model: software architecture and performance. In: Mozdzynski G (ed) Proceedings of the 11th ECMWF Workshop on the Use of High Performance Computing In Meteorology, 25–29 October 2004, Reading, UK

Moon I-J (2005) Impact of a coupled ocean wave–tide–circulation system on coastal modeling. Ocean Model 8(3):203–236. doi:10.1016/j.ocemod.2004.02.001

Moon J-H, Hirose N, Yoon J-H, Pang I-C (2010) Offshore detachment process of the low-salinity water around Changjiang Bank in the East China Sea. J Phys Oceanogr 40(5):1035–1053. doi:10.1175/2010JPO4167.1

Olabarrieta M, Warner JC, Armstrong B, Zambon JB, He R (2012) Ocean–atmosphere dynamics during Hurricane Ida and Nor'Ida: an application of the coupled ocean–atmosphere–wave–sediment transport (COAWST) modeling system. Ocean Model 43-44(C):112–137. doi:10.1016/j.ocemod.2011.12.008

Onken R, Robinson AR, Kantha L, Lozano CJ, Haley PJ, Carniel S (2005) A rapid response nowcast/forecast system using multiply nested ocean models and distributed data systems. J Mar Syst 56(1–2):45–66. doi:10.1016/j.jmarsys.2004.09.010

Pawlowicz R, Beardsley B, Lentz S (2002) Classical tidal harmonic analysis including error estimates in MATLAB using T_TIDE. Comput Geosci 28:929–937

Penven P, Debreu L, Marchesiello P, McWilliams JC (2006) Evaluation and application of the ROMS 1-way embedding procedure to the central California upwelling system. Ocean Model 12:157–187

Powell BS, Moore AM, Arango HG, Di Lorenzo E, Milliff RF, Leben RR (2009) Near real-time ocean circulation assimilation and prediction in the Intra-Americas Sea with ROMS. Dyn Atmos Oceans 48(1–3):46–68. doi:10.1016/j.dynatmoce.2009.04.001

Qi JC, Chen RC, Beardsley WP, Cowles G (2009) An unstructured-grid finite-volume surface wave model (FVCOM-SWAVE): implementation, validations and applications. Ocean Model 28:153–166. doi:10.1016/j.ocemod.2009.01.007

Qiao F, Yang Y, Lu X, Xia C, Chen X, Wang B, Yuan Y (2006) Coastal upwelling in the East China Sea in winter. J Geophys Res 111, C11S06. doi:10.1029/2005JC003264

Sasaki H, Siswanto E, Nishiuchi K, Tanaka K, Hasegawa T, Ishizaka J (2008) Mapping the low salinity Changjiang Diluted Water using satellite-retrieved colored dissolved organic matter (CDOM) in the East China Sea during high river flow season. Geophys Res Lett 35(4):L04604

Schmidt A, Gangopadhyay A (2012) An operational ocean circulation prediction system for the western North Atlantic Hindcasting during July–September of 2006. Cont Shelf Res 1–16. doi:10.1016/j.csr.2012.08.017

Skamarock WC, Klemp JB, Dudhia J, Gill DO, Baker DM, Duda MG, Huang X-Y, Wang W, Powers JG (2008) A description of the advanced research WRF version 3. NCAR technical note, NCAR/TN-475+STR, p 125

Svendsen IA (1984) Mass flux and undertow in the surf zone. Coast Eng 8:347–366

Svendsen IA, Haas K, Zhao Q (2002) Quasi-3D nearshore circulation model SHORECIRC, user's manual, draft report. Center for Applied Coastal Research, Department of Civil Engineering, University of Delaware, Newark

Warner J, Sherwood C, Signell R, Harris C, Arango H (2008) Development of a three-dimensional, regional, coupled wave, current, and sediment-transport model. Comput Geosci 34(10):1284–1306

Warner JC, Armstrong B, He R, Zambon JB (2010) Development of a coupled ocean–atmosphere–wave–sediment transport (COAWST) modeling system. Ocean Model 35(3):230–244. doi:10.1016/j.ocemod.2010.07.010

Watanabe M (2007) Simulation of temperature, salinity and suspended matter distributions induced by the discharge into the East China Sea during the 1998 flood of the Yangtze River. Estuarine Coastal Shelf Sci 71(1–2):81–97

Weisberg RH, Barth A, Alvera-Azcárate A, Zheng L (2009) A coordinated coastal ocean observing and modeling system for the West Florida Continental Shelf. Harmful Algae 8(4):585–597. doi:10.1016/j.hal.2008.11.003

Wu H, Zhu J, Shen J, Wang H (2011a) Tidal modulation on the Changjiang River plume in summer. J Geophys Res 116:C08017. doi:10.1029/2011JC007209

Wu L, Chen C, Guo P, Shi M, Qi J, Ge J (2011b) A FVCOM-based unstructured grid wave, current, sediment transport model, I. Model description and validation. J Ocean Univ China (Ocean Coast Sea Res). doi:10.1007/s11802-011-1788-3

Zheng L, Weisberg RH (2012) Modeling the west Florida coastal ocean by downscaling from the deep ocean, across the continental shelf and into the estuaries. Ocean Model 48(C):10–29. doi:10.1016/j.ocemod.2012.02.002

Zhu J, Chen C, Ding P, Li C, Lin H (2004) Does the Taiwan warm current exist in winter? Geophys Res Lett 31:L12302. doi:10.1029/2004GL019997